Structural model of an mRNA in complex with the bacterial chaperone Hfq

Yi Peng[a], Joseph E. Curtis[b], Xianyang Fang[c], and Sarah A. Woodson[d,1]

[a]Cell, Molecular and Developmental Biology and Biophysics Program, Johns Hopkins University, Baltimore, MD 21218; [b]Center for Neutron Research, National Institute of Standards and Technology, Gaithersburg, MD 20899; [c]Structural Biophysics Laboratory, Center for Cancer Research, National Cancer Institute, National Institutes of Health, Frederick, MD 21702; and [d]T. C. Jenkins Department of Biophysics, Johns Hopkins University, Baltimore, MD 21218

Edited by Jennifer A. Doudna, University of California, Berkeley, CA, and approved October 20, 2014 (received for review May 30, 2014)

The Sm-like protein Hfq (host factor Q-beta phage) facilitates regulation by bacterial small noncoding RNAs (sRNAs) in response to stress and other environmental signals. Here, we present a low-resolution model of *Escherichia coli* Hfq bound to the *rpoS* mRNA, a bacterial stress response gene that is targeted by three different sRNAs. Selective 2′-hydroxyl acylation and primer extension, small-angle X-ray scattering, and Monte Carlo molecular dynamics simulations show that the distal face and lateral rim of Hfq interact with three sites in the *rpoS* leader, folding the RNA into a compact tertiary structure. These interactions are needed for sRNA regulation of *rpoS* translation and position the sRNA target adjacent to an sRNA binding region on the proximal face of Hfq. Our results show how Hfq specifically distorts the structure of the *rpoS* mRNA to enable sRNA base pairing and translational control.

small noncoding RNA | RNA–protein interactions | SAXS | Lsm protein | bacterial posttranscriptional control

The bacterium *Escherichia coli* encodes 80 small noncoding RNAs (sRNAs) that fine-tune gene expression for different growth environments, increasing survival under various stress conditions (1, 2). Base pairing between an sRNA and an mRNA can inhibit gene expression by masking the ribosome binding site or by increasing mRNA turnover (3). Alternatively, sRNAs increase translation by changing the mRNA structure and exposing the ribosome binding site. In *E. coli*, sRNA regulation depends on Hfq (host factor Q-beta phage), a protein that stabilizes and accelerates base pairing between many known sRNAs and their mRNA targets (3, 4).

Hfq belongs to the Sm/Lsm protein family (5) and recognizes diverse RNA targets by three distinct RNA binding surfaces (6). The distal face of the Sm ring binds AAN triplets (7, 8) present in many mRNA targets of sRNA regulation (9). The inner surface of the proximal face binds U-rich single strands (10, 11), which are a common feature of bacterial sRNA terminators and important for Hfq action (12, 13). Finally, a patch of conserved basic residues (R16, R17, R19, and K47) on the rim interacts with internal U-rich sequences in sRNAs, increasing the accessibility of the seed region (14) and catalyzing base pairing between complementary strands (15).

Although Hfq is known to bind specific sequences in sRNAs and mRNAs, how it restructures its targets for translational control is not understood. We address this question using *E. coli rpoS*, a well-studied target of posttranscriptional regulation by sRNAs and Hfq. *rpoS* encodes σ^S, a major stress-response regulator that is up-regulated by DsrA, RprA, and ArcZ sRNAs in *E. coli* (16). Genetic experiments showed that an inhibitory stem loop in the *rpoS* mRNA blocks ribosome binding; sRNAs open this inhibitory stem by base pairing to its upstream strand (17, 18). Hfq must be recruited to an $(AAN)_4$ motif in an upstream domain of the *rpoS* mRNA to facilitate sRNA base pairing and regulation (19, 20). Biochemical experiments showed that Hfq interacts weakly with the *rpoS* inhibitory stem loop, cycling off the sRNA–mRNA antisense duplex as it is formed (21). These experiments left unanswered why Hfq must interact with two domains of the *rpoS* mRNA, how it remodels the *rpoS* mRNA to seed base pairing by a complementary sRNA (22), and why sRNA binding displaces Hfq from the inhibitory stem loop.

Here, we show that Hfq enables sRNA regulation by folding the *rpoS* mRNA leader into a specific tertiary structure that partially unwinds the inhibitory stem and poises Hfq to bring both RNAs together. Small-angle X-ray scattering (SAXS), functional assays, and SHAPE (selective 2′-hydroxyl acylation and primer extension) footprinting revealed that Hfq contacts three distinct sites in the *rpoS* mRNA, folding the 5′ leader of the *rpoS* mRNA into a compact structure. Three-dimensional models of the *rpoS*•Hfq complex refined against the SAXS data show that the two domains of the *rpoS* mRNA wrap around the Hfq hexamer, placing the inhibitory stem over the arginine patch and adjacent to the sRNA binding sites on the rim and proximal face. These results demonstrate that multiple RNA binding surfaces on Hfq enable the protein to distort the structure of the *rpoS* mRNA, poising the complex for sRNA entry and translation.

Results

Hfq Binds A-Rich and U-Rich Motifs in *rpoS* mRNA. We used SHAPE footprinting to identify Hfq interaction sites in the *rpoS* leader RNA. Previous experiments showed that the $(AAN)_4$ motif upstream of the sRNA target site binds the distal face of the Hfq and recruits Hfq to the *rpoS* mRNA (20, 22, 23). Hfq has the potential to also interact with a "U_5" loop motif (5′ UUAUUU) downstream of the sRNA target site (21, 24).

For footprinting experiments, we used *rpoS301*, a 284-nt variant of the 576-nt *rpoS* leader that lacks a nonessential upstream

Significance

Small noncoding RNAs optimize bacterial gene expression under stress and increase the virulence of many bacterial pathogens. The RNA-binding protein Hfq (host factor Q-beta phage) promotes base pairing between small RNAs and target mRNAs, but it is not known how Hfq brings the two RNAs together in the proper orientation. We used chemical footprinting, small-angle X-ray scattering, and molecular dynamics simulations to model the structure of Hfq bound to an mRNA in solution. The surprising result is that the mRNA wraps entirely around the Hfq protein, specifically contacting both surfaces. This destabilizes the mRNA structure around the small RNA target site, poising it to base pair with a complementary small RNA also bound to Hfq.

Author contributions: Y.P. and S.A.W. designed research; Y.P. and J.E.C. performed research; Y.P., J.E.C., and X.F. contributed new reagents/analytic tools; Y.P., J.E.C., and X.F. analyzed data; and Y.P. and S.A.W. wrote the paper.

The authors declare no conflict of interest.

This article is a PNAS Direct Submission.

[1]To whom correspondence should be addressed. Email: swoodson@jhu.edu.

This article contains supporting information online at www.pnas.org/lookup/suppl/doi:10.1073/pnas.1410114111/-/DCSupplemental.

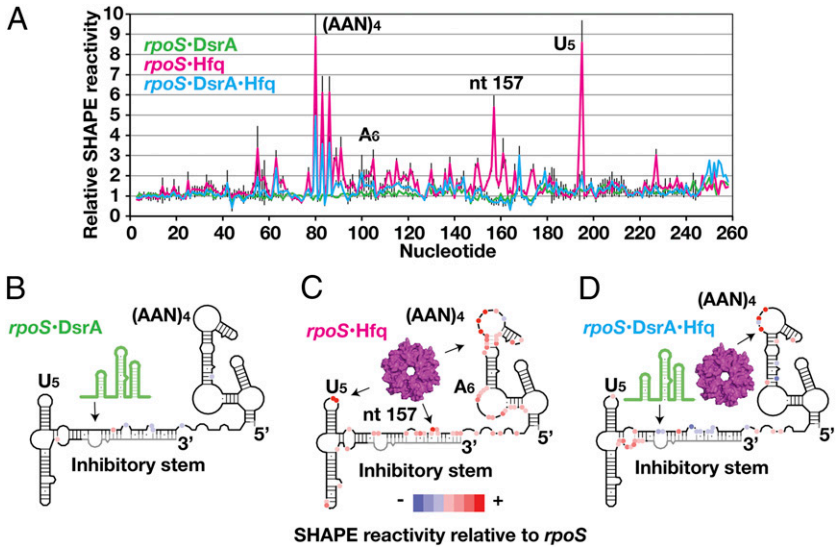

Fig. 1. Conformational changes in *rpoS* mRNA from binding of DsrA and Hfq. (*A*) SHAPE reactivity of 50 nM *rpoS301* RNA in complex with 200 nM DsrA (green trace), 333 nM Hfq (magenta), or DsrA and Hfq (blue) relative to *rpoS* RNA alone (Fig. S1). $(AAN)_4$ motif, nucleotides 77–88; inhibitory stem, nucleotides 149–184 and 249–284; U_5 motif, nucleotides 192–197. NMIA modification was carried out at 37 °C (*Materials and Methods*) and the extent of modification was measured by primer extension (Fig. S1*C*). Error bars represent ±SD for at least three independent experiments. (*B–D*) Schematic of SHAPE reactivity relative to free *rpoS* RNA for each complex, from a histogram of the entire dataset (Fig. S1*D*). Red circles, nucleotides with enhanced SHAPE reactivity; blue circles, nucleotides with reduced SHAPE reactivity; black line, regions with unchanged SHAPE reactivity; gray line, regions with no SHAPE data. Arrows indicate DsrA and Hfq binding regions in *rpoS* RNA.

domain but retains the Hfq binding domain and inhibitory stem needed for translational control and Hfq and sRNA binding (24). The *rpoS301* RNA folds homogeneously in vitro and retains the native secondary structure (Fig. S1 *A* and *B*) based on its similar SHAPE modification as the full-length *rpoS* leader (24). We compared the SHAPE modification levels of free *rpoS301* RNA with *rpoS301* RNA bound to DsrA sRNA or to Hfq (Fig. 1*A* and Fig. S1*C*). We then categorized the decrease or increase in relative SHAPE reactivity based on a histogram of the entire dataset (Fig. S1*D*), which reflects a change in the accessibility of the ribose 2′OH or the flexibility of the RNA backbone (25).

As expected, base pairing between *rpoS* mRNA and DsrA sRNA protected the DsrA binding site in the inhibitory stem from modification, reducing the SHAPE reactivity by ∼30–40% (Fig. 1*B*). The SHAPE reactivity of the upstream and downstream domains did not change appreciably, however, suggesting they are unaffected by DsrA (green trace in Fig. 1 *A* and *B*).

By contrast, Hfq remodeled the *rpoS* mRNA structure extensively (magenta trace in Fig. 1 *A* and *C*). First, the reactivity of the inhibitory stem and the helix connecting the $(AAN)_4$ and A_6 motifs increased two- to threefold over that of the free RNA. These residues were uniformly and moderately modified in the *rpoS*•Hfq complex, suggesting that Hfq partially opens the mRNA secondary structure. An Hfq-induced structural change in the inhibitory stem was also reported based on RNase footprinting experiments (26).

Second, Hfq binding resulted in unusually strong modification of three regions that we deduced make specific contacts with Hfq: the $(AAN)_4$ motif previously known to bind Hfq, the U_5 motif in the downstream domain, and A157 in the inhibitory stem near the 5′ end of the sRNA target site. The first A of every AAN triplet was four to nine times more modified in the Hfq complex than in the RNA control (A80, A83, and A85 in Fig. 1*A*) (also Fig. S1*C*). This hyperreactivity was explained by a structure showing that the A-specific pocket on the distal face

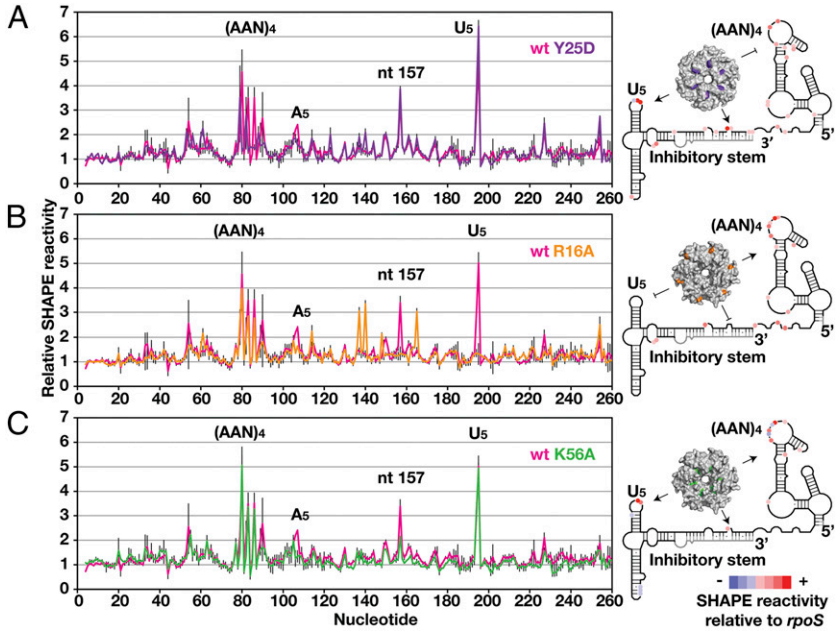

Fig. 2. Mapping *rpoS* interaction sites on Hfq. (*Left*) SHAPE modification of *rpoS* RNA in complex with wt Hfq (pink trace) or an RNA binding surface mutation. Error bars are as in Fig. 1. (*A*) Distal face Y25D mutation (purple) disrupts Hfq binding to $(AAN)_4$ motif. (*B*) Rim R16A mutation (orange) disrupts Hfq binding to inhibitory stem and U_5 motif. (*C*) Proximal face K56A mutation (green) retained the three direct binding sites, but did not appreciably change the RNA secondary structure.

BIOCHEMISTRY

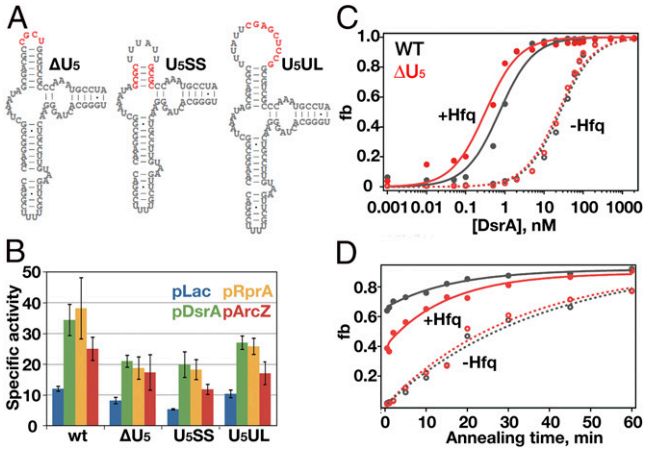

Fig. 3. Function of U_5 motif in sRNA binding and regulation. (*A*) Mutations in the U_5 motif (red) delete the U-rich sequence in the loop (ΔU_5), shorten the helix (U_5SS), or insert a GC-rich sequence in the loop (U_5UL). (*B*) β-Galactosidase activity assays measure translation of *rpoS::lacZ* in *E. coli* when sRNAs are overexpressed from IPTG-inducible plasmids. Empty pLac vector (blue), pDsrA (green), pRprA (orange), and pArcZ (red) are shown. (*C* and *D*) DsrA binding to WT *rpoS* RNA (gray) and ΔU_5 *rpoS* RNA (red) without Hfq (open circles and dashed lines) or with Hfq (solid circles and solid lines). Binding was measured by native gel mobility shift (Fig. S2 *C* and *D*). (*C*) Equilibrium binding. A fraction of *rpoS*•DsrA (RD) or *rpoS*•DsrA•Hfq (RDH) vs. [DsrA] was fitted to a single-site binding isotherm. (*D*) *rpoS*-DsrA annealing kinetics. Data were fitted to single- (no Hfq) or double- (+Hfq) exponential equations (20). Error bars represent ±SD for at least three independent experiments.

of *E. coli* Hfq (7) locks the ribose into a highly reactive C2′-endo conformation (27). The third and fourth residues in the U_5 motif were also eight times more modified in the *rpoS*•Hfq complex (A194 and U195 in Fig. 1*A*) (Fig. S1*C*, *Bottom Left*), indicating that Hfq also interacts with this U-rich loop as suggested by previous RNase footprinting experiments (21). Finally, A157 in the inhibitory stem was six times more reactive in the *rpoS*•Hfq complex (Fig. 1*A*), pointing to a previously unsuspected interaction between Hfq and the start of the inhibitory stem.

When both DsrA and Hfq were added, the modification pattern of the DsrA•*rpoS*• Hfq ternary complex showed that Hfq releases the inhibitory stem and U_5 motif but remains bound to the upstream $(AAN)_4$ motif (Fig. 1*D*). This is consistent with in vitro annealing experiments showing that Hfq cycles off the sRNA–mRNA duplex after the RNAs have base paired (21). The DsrA target site was ~50–80% less modified in the ternary complex than in the DsrA•*rpoS* complex (Fig. 1*D*), consistent with tighter DsrA•*rpoS* binding in the presence of Hfq (19). Meanwhile, nucleotides upstream of the Shine–Dalgarno sequence became two- to threefold more accessible in the ternary complex.

A U_5 Motif Binds the Lateral Rim of Hfq. To test which surfaces of Hfq contact *rpoS* mRNA, we repeated the SHAPE experiments with Hfq mutants Y25D, R16A, and K56A that disrupt RNA binding to the distal face, the lateral rim, and the proximal face, respectively (8, 14, 28). As expected, the Y25D mutation selectively disturbed the hypermodification of the $(AAN)_4$ motif (Fig. 2*A*), consistent with its binding to Hfq's distal face (7, 22). Binding was only partially impaired by the Y25D mutation, as it eliminated the hyperreactivity of only the third (AAN) triplet and shifted the modification pattern 1 nt upstream (Fig. 2*A*, purple trace). The SHAPE reactivities of the inhibitory stem and the downstream domain were the same as in the WT Hfq complex, indicating that those regions interact with a different surface of Hfq.

Strikingly, the R16A rim mutation abolished interactions with the inhibitory stem and the U_5 motif while leaving intact interactions with the $(AAN)_4$ motif (Fig. 2*B*, orange trace). The lost hypermodification of the U_5 motif (A194 and U195) suggested that this loop directly contacts the lateral rim of Hfq. Modification of A157 returned to the average level, and modification of C137, C140, and C165 increased approximately threefold (Fig. 2*B*, orange and gray traces), indicating that the perturbed interaction with the rim also changed the conformation of the inhibitory stem. Finally, the K56A mutant did not appreciably change the modification pattern (Fig. 2*C*), confirming that the proximal face of Hfq does not bind *rpoS* mRNA directly.

U_5 Motif Binding at Hfq Rim Facilitates DsrA Annealing. The SHAPE results showed that the lateral rim of Hfq contacts the downstream U_5 motif in the *rpoS* mRNA leader, whereas the distal face remains bound to the upstream $(AAN)_4$ motif. To investigate whether the U_5 motif is required for regulation of *rpoS* translation by Hfq and sRNAs, we replaced the UUAUUU loop with UCGC (Fig. 3*A*, ΔU_5), shortened the stem by 3 bp (Fig. 3*A*, U_5SS), or enlarged the loop by 9 nt (Fig. 3*A*, U_5UL).

All three mutations in the U_5 stem loop diminished the ability of DsrA and RprA sRNAs to up-regulate expression of full-length *rpoS*::lacZ fusions in the *E. coli* chromosome by 20–40% (Fig. 3*B*, green and gold bars). The magnitude of this effect was similar to that of mutating the upstream $(AAN)_4$ and A_6 motifs (Fig. S2*A*, Δ2), although the U_5 mutations had a smaller effect on up-regulation by ArcZ sRNA (Fig. 3*B*, red bars). When the $(AAN)_4$, A_6, and U_5 motifs were all mutated, expression of *rpoS::lacZ* fusions was reduced a further 50% (compare Δ2 and Δ3 in Fig. S2 *A* and *B*), showing that the $(AAN)_4$, A_6, and U_5 motifs not only interact with different surfaces of Hfq, but also make distinct contributions to the regulation of *rpoS* translation by sRNAs and Hfq.

To investigate whether the U_5 motif is important for DsrA annealing in vitro, we next measured the stability of the DsrA•*rpoS* complex, using native gel mobility shift assays (Fig.

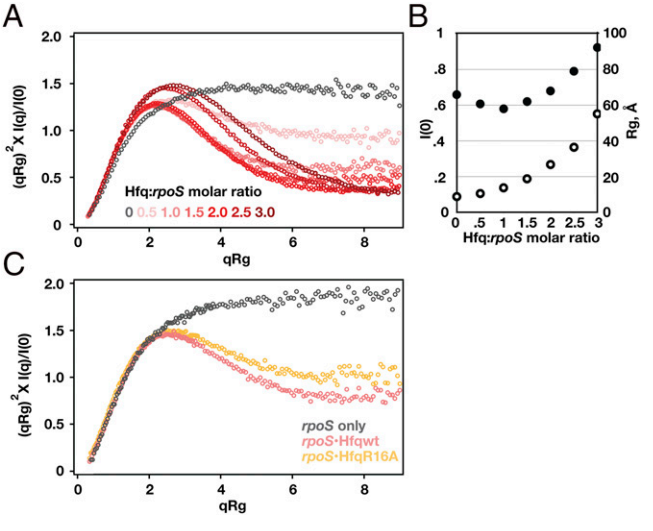

Fig. 4. SAXS of rpoS•Hfq complexes reveals a compact structure. (*A*) Dimensionless Kratky plot (31) of SAXS profiles for *rpoS* RNA alone (black) and *rpoS*•Hfq complexes at increasing protein:RNA ratios (pink to red). Bell-shaped curves indicate compact structures. See Fig. S4 and Table S2 for further data. (*B*) Hfq binding increased I(0) (open circles) and decreased R_g (solid circles) compared with free *rpoS* RNA. At 1:1 mol ratio, ~95% of RNA is bound to Hfq. Correction for scattering from the free RNA and protein reduces the experimental R_g of the complex by ~1 Å. (*C*) Kratky plots of *rpoS* RNA alone (black), with 1:1 WT Hfq (pink) and with 1:1 Hfq:R16A (gold).

S2 *C* and *D*) (19). We titrated ^{32}P-labeled *rpoS* mRNA with DsrA sRNA (0–2 μM) and quantified the total fraction of *rpoS*•DsrA and *rpoS*•DsrA•Hfq complexes as a function of DsrA concentration (Fig. 3*C*). Without Hfq, the ΔU_5 mutation did not change the strength of the DsrA–*rpoS* RNA interaction, suggesting that this mutation does not alter the structure of free *rpoS* mRNA (Table S1). With Hfq present, however, DsrA bound the ΔU_5 complex about twofold better than the WT *rpoS*•DsrA•Hfq complex, perhaps owing to better release of the downstream domain (Table S1).

We next measured the ability of Hfq to increase the rate of DsrA annealing with *rpoS* mRNA (Fig. 3*D*). Without Hfq, both WT and ΔU_5 *rpoS* mRNA base paired with DsrA at the same rate (0.03 min^{-1}). In the presence of Hfq, however, a lower proportion of ΔU_5 than WT *rpoS* mRNA annealed with DsrA during the first 30 s (Table S1). Thus, these results suggest that interactions between Hfq and the U_5 motif distort the *rpoS* mRNA conformation for efficient DsrA entry.

Further SHAPE footprinting results on the ΔU_5 mRNA confirmed that this defect in DsrA annealing was due to impaired Hfq binding at the U_5 motif, based on the loss of hyperreactivity at this position (Fig. S3*A*). The ΔU_5 mutation also lowered modification of the upstream $(AAN)_4$ motif by ~80%, consistent with an overall reduction in Hfq affinity (24). Surprisingly, we still observed strong modification of A157 in the inhibitory stem, suggesting this contact depends on recruitment of Hfq by the $(AAN)_4$ motif rather than U_5 motif. The SHAPE reactivity of the inhibitory stem was no longer enhanced, however, consistent with our previous conclusion that the U_5 motif is needed for Hfq to open the inhibitory stem. The U_5SS and U_5UL mutations also disrupted Hfq binding at the U_5 motif (Fig. S3 *B* and *C*) and reduced in vivo expression of *rpoS::lacZ*.

Hfq Folds *rpoS* mRNA. If the distal face of Hfq binds the upstream $(AAN)_4$ motif while the lateral rim interacts with the downstream U_5 motif, Hfq binding likely alters the tertiary conformation of the *rpoS* mRNA. To test that hypothesis, we used SAXS to compare the global shape of free *rpoS* RNA and the *rpoS*•Hfq complex in solution, at molar ratios from 1:0.5 to 1:3 RNA:Hfq$_6$ (Fig. 4). The scattering profile of free Hfq protein (Fig. S4 *A* and *B*) was consistent with its known structure as previously reported (29, 30). The scattering profile of the free *rpoS* mRNA (284 nt) revealed an extended structure with radius of gyration (R_g) = 68.1 ± 0.6 Å (Fig. S4 *C* and *D*). A dimensionless Kratky plot (31) of the scattering intensity exhibited the plateau at higher-momentum transfer (q), indicating an extended or flexible conformation (Fig. 4*A*, black symbols).

The shape of the Kratky scattering curves changed dramatically when Hfq was added, forming the symmetric maximum characteristic of globular particles (Fig. 4*A*, red symbols). This change in shape corresponded with a drop in R_g (Fig. 4*B*, solid circles) despite the greater mass of the *rpoS*•Hfq complex (Fig. 4*B*, open circles). The smallest R_g value of 58 ± 1 Å was reached at 1:1 r*poS*:Hfq$_6$ (Fig. S4 *E* and *F*), at which concentration 95% of the RNA is expected to be bound with Hfq (24). The change in the scattering profile cannot be explained by scattering from the protein alone, as Hfq has a much smaller X-ray scattering contrast than the RNA (Fig. S4*E*). Instead, we inferred that the flexible *rpoS* leader must adopt a more compact tertiary structure when bound to Hfq. This compact structure is stabilized by interactions between *rpoS* mRNA and the rim of Hfq, because the Hfq:R16A mutant formed a more extended complex with *rpoS* mRNA than did WT Hfq (Fig. 4*C*, gold symbols).

Structure Models of *rpoS* and Hfq. We next used the SAXS and SHAPE footprinting results to model the 3D structures of the free *rpoS* mRNA and the *rpoS*•Hfq complex. Molecular envelopes calculated ab initio from the SAXS data revealed an elongated "L" for the free *rpoS* RNA (Fig. S5*A*), which curled inward when Hfq was present (Fig. S5*B*). Nevertheless, many structural features were lost when these envelopes were averaged, presumably because the RNA is flexible and poorly constrained by the scattering curves. In addition, Hfq was nearly invisible in the molecular envelopes, owing to its lower scattering contrast relative to the RNA. Therefore, we used rigid-body methods to build atomistic models of the *rpoS*•Hfq complex, using the information available from SAXS, crystal structures, and biochemical footprinting. Although these data cannot specify the conformation of individual residues, we obtained low-resolution models that were consistent with all of the available

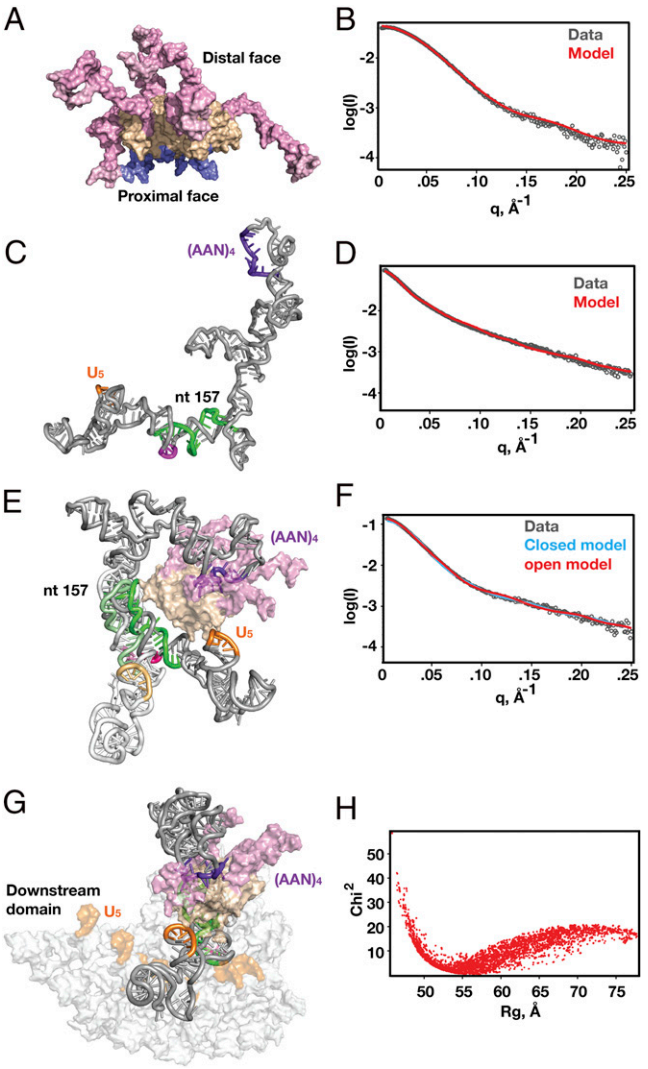

Fig. 5. Model of the *rpoS* RNA•Hfq regulatory complex. Shown are all-atom models of (*A* and *B*) full-length Hfq, (*C* and *D*) *rpoS* RNA, and (*E* and *F*) *rpoS*•Hfq complex. The U_5-rim contact was constrained in the closed model (SASREF) (35); the open model is from the SASSIE (33) trajectory. Hfq is rendered as a surface; Sm core [residues (res) 6–65], wheat color; N termini (res 1–5), slate color; C termini (res 66–102), pink. *rpoS* RNA ribbon, gray; $(AAN)_4$ motif, purple; U_5 motif, orange; sRNA binding site, green; Shine–Dalgarno site, violet. See Fig. S7 for details of the RNA model. (*B*, *D*, and *F*) Scattering curves predicted by models (red or blue) compared with experimental scattering (gray) for (*B*) full-length Hfq, (*D*) *rpoS* RNA, and (*F*) *rpoS*•Hfq complex in closed or open conformation. (*G*) Open structures from SASSIE. The best-fitting 917 models from the trajectory (*H*) were clustered (UCSF Chimera), and each cluster is represented by a semitransparent surface to illustrate the wedge of conformations that describe the scattering curve.

data and that suggested how Hfq enables sRNA regulation of *rpoS* translation.

We first built an all-atom model of the full-length *E. coli* Hfq hexamer by appending disordered N- and C-terminal residues to a crystallographic model of the stable Sm core [Protein Data Bank (PDB) ID: 4HT8] (32). We used the program SASSIE (33) to simulate conformations of the N and C termini that fitted the experimental SAXS data (Fig. S6*A*). In the best structures, the N termini (amino acids 1–5) projected from the center of the proximal face (Fig. 5*A*, purple), whereas the C termini were mostly oriented toward the distal face (Fig. 5*A*, pink). This distal orientation differs from the radial projection of the C termini in previous ab initio models (30) (Fig. S5*C*).

To model the tertiary structure of the free *rpoS* mRNA, we divided the *rpoS301* sequence into six fragments, using our SHAPE-determined secondary structure as a guide (Fig. S7*A*). We generated structures for each fragment with MC-Sym (34) and arranged the fragments in space by rigid-body modeling (SASREF) (35) against the experimental SAXS data (Fig. S7*B* and *SI Materials and Methods*). In the resulting model, the upstream and inhibitory domains again form an L connected by a flexible hinge at nucleotides 128–129 (Fig. 5*C*). Because these domains likely sample different orientations in solution, we used this hinge as a pivot point in a SASSIE Monte Carlo simulation, which generated an ensemble of 27,427 structures spanning the experimental R_g (Fig. S6*B*). The best-fit structures from this ensemble resembled the initial L-shaped model.

Structural Models of the *rpoS*•Hfq Complex. We repeated this modeling procedure to visualize the structure of the *rpoS*•Hfq complex, using the scattering data from the 1:1 *rpoS*:Hfq_6 sample as an experimental constraint. We used a crystallographic structure of the Hfq core bound to rA_7 (32) to model the interaction between the $(AAN)_4$ motif and the distal face of Hfq. In addition, as our SHAPE data showed that the *rpoS* U_5 motif and A157 in the inhibitory stem both interact with the rim of Hfq, we constrained those residues to be within 7 Å of R16 in any Hfq monomer.

The resulting model (Fig. 5 *E* and *F*) showed the *rpoS* mRNA wrapped around the Hfq hexamer, with the U_5 motif on the proximal side of the rim opposite the second AAN triplet and A157 at the rim on the other side of the ring. Strikingly, this orientation projected the inhibitory stem across the proximal face of Hfq, with the sRNA complementary strand toward Hfq and the ribosome binding site away from Hfq. This wrapped structure necessitates a slight unwinding of the inhibitory stem, consistent with the moderate increase in SHAPE modification of this region when Hfq binds. Hfq may induce additional RNA conformational changes that are not captured by our rigid-body modeling procedure. Overall, the model explained how Hfq folds the *rpoS* mRNA into a more compact structure and why interactions with both the AAN motif and the U_5 motif are needed for efficient sRNA entry.

To determine whether other conformations also fit the SAXS data, we used SASSIE to vary the orientation of the downstream RNA domain about the flexible hinge (nucleotides 128–129). Structures of the *rpoS*•Hfq complex that best represent the data ($\chi^2 < 1.5$; 917 structures) were symmetrically distributed about R_g = 55 Å (Fig. 5*H*) and collectively sampled a restricted wedge of space that could reflect an oscillatory path of the inhibitory stem in which the U_5 motif detaches and rebinds the Hfq lateral rim (Fig. 5*G* and Fig. S6*D*). This ensemble of "open" structures described the scattering data nearly as well as the initial "closed" structure (Fig. 5*F*). In all of these structures, nucleotide A157 remained close to the Hfq rim, consistent with our SHAPE data showing that hypermodification of this residue in the inhibitory stem depends on the $(AAN)_4$ motif binding rather than the U_5 motif. By contrast, the sRNA annealing site, the ribosome binding site, and the U_5 motif moved away from Hfq in the more open structures.

Discussion

Our SHAPE footprinting results, SAXS data, and all-atom models collectively show that Hfq folds the *rpoS* mRNA leader into a compact tertiary structure. This folded structure positions the inhibitory stem of the *rpoS* leader over the proximal face of Hfq where sRNAs are known to bind. This unexpected result explains many features of *rpoS* regulation by sRNAs and Hfq, such as how Hfq brings together the complementary regions of the mRNA and sRNA near the arginine patches along the rim and why sequences upstream and downstream of the sRNA target site are important. Moreover, our SHAPE results show that Hfq partially opens the secondary structure of the inhibitory stem to enhance sRNA annealing and ribosome binding (22, 26). Remodeling of the *rpoS* mRNA requires interactions with both $(AAN)_4$ and U_5 motifs.

As the SAXS data do not provide information about local structure, our model cannot capture the details of the RNA–Hfq interactions. Moreover, the model does not account for local perturbations to the RNA structure. Nevertheless, the overall arrangement of the *rpoS* mRNA leader with respect to Hfq in our model is well supported by experimental data. First, the dramatic change in the scattering function provides direct physical evidence for compaction of the RNA by Hfq. Second, the marked change in RNA backbone modification (SHAPE) in response to the Hfq and ΔU_5 mutations is consistent with specific Hfq interactions, rather than nonspecific effects of the protein on the RNA structure. Unusually strong ribose modification may serve as a diagnostic for direct Hfq–RNA interactions. Third, mutational studies showed that the position and orientation of the $(AAN)_4$ and U_5 sequences are important for Hfq-mediated sRNA regulation, suggesting they bind Hfq simultaneously (Fig. S3) (24). Finally, an unbiased search of structural models indicated that only a subset of RNA conformations recapitulates the SAXS data (Fig. 5 *G* and *H* and Fig. S6*D*).

Our data show that Hfq folds the *rpoS* leader into a compact, closed conformation by simultaneously recognizing an upstream $(AAN)_4$ motif and downstream U_5 motif flanking the sRNA target site. In this closed mode, the inhibitory stem is partially melted, and the 5′ end of the target site interacts with the Hfq rim where we propose the arginine patch promotes base pairing with a complementary sRNA. The SHAPE data show that Hfq disengages from the downstream U_5 motif after a sRNA base pairs with the inhibitory stem, while remaining bound to the $(AAN)_4$ motif. The potential to form more open structures explains how the *rpoS* leader can flex to allow Hfq to cycle off the DsrA–*rpoS* duplex, exposing the ribosome binding site.

The potential for opening and closing the *rpoS*•Hfq complex is clearly captured in our structural models. The closed *rpoS*•Hfq model obtained by constraining the U_5 motif to interact with the Hfq rim was reasonably consistent with the SAXS data. However, the Monte Carlo simulations showed that more open structures fitted the scattering data equally well, even assuming a small fraction of free RNA. The *rpoS*•Hfq complex may fluctuate between open and closed conformations in solution. As the scattering curves for 2:1 Hfq:*rpoS* also indicate a folded structure, our data do not exclude models in which the open *rpoS* leader binds a second Hfq hexamer.

Although AAN sequences are known to recruit Hfq via its distal face (7, 8, 20), here we find that the U_5 motif in *rpoS* also contributes to sRNA annealing by interacting with the Hfq rim. This distorts the mRNA structure, making it more accessible to sRNAs (22). Multilateral Hfq interactions may be widespread among bacterial sRNA–mRNA pairs and important for regulation. The *fhlA* mRNA leader was proposed to contact both distal and proximal faces of Hfq based on competitive binding experiments (36). Hfq inhibits translation of *cirA* by binding to an upstream (AAN) motif and two U-rich patches close to the Shine–Dalgarno sequence (37), raising the possibility that Hfq

also folds the *cirA* mRNA for translational control. Our results show that Hfq forms a specific, folded *rpoS* mRNP that spring loads the regulatory helix for sRNA entry.

Materials and Methods

SHAPE Footprinting. Complexes of 50 nM *rpoS301* RNA, 333 nM *E. coli* Hfq hexamer, and 200 nM DsrA sRNA were prepared as previously described (24) in 10 μL annealing buffer [50 mM Tris·HCl, pH 7.5, 50 mM NaCl, 50 mM KCl, 50 mM NH_4Cl, 2% (vol/vol) glycerol] at 25 °C for 2 h. Complexes were modified with *N*-methylisatoic anhydride (Molecular Probes) and analyzed by reverse transcription as described in *SI Materials and Methods*. Reported values of relative SHAPE reactivities are the average of at least three independent experiments.

Hfq Binding and Translational Activation. *E. coli* strains and β-galactosidase assays of *rpoS::lacZ* expression were performed as previously described (19, 24). Gel mobility shift binding assays with ~70 nM ^{32}P-labeled *rpoS301* RNA and DsrA or Hfq were performed in annealing buffer for 2 h at 25 °C as previously described (20, 24) before native 6% polyacrylamide gel electrophoresis in 66 mM Hepes, 34 mM Tris, 0.1 mM EDTA, and 2 mM $MgCl_2$.

SAXS. *rpoS301* RNA and Hfq protein were prepared under native conditions as described in *SI Materials and Methods*. Small-angle X-ray scattering data were collected at room temperature at the Advanced Photon Source 12-ID-B, over the range $0.005 < q < 1.007$ Å^{-1} after background subtraction. Data collected at three different sample concentrations showed the expected increase in I(0) and constant R_g and ratios of scattering intensity, indicating a lack of interparticle interactions (Fig. S4). Parameters of the fits and estimates of the particle mass are listed in Table S2.

Structural Models. Three-dimensional models of *rpoS* mRNA secondary structure fragments (Fig. S7) were generated using MC-Sym web server (34) and oriented in three dimensions with SASREF (35), using the RNA chain connectivity and the SAXS experimental data as constraints. CORAL was used to model the full *rpoS*•Hfq complex against the SAXS data for the 1:1 RNA:Hfq sample (35). In the complex, *rpoS* P 195 (U_5 motif) and P 157 (inhibitory stem) were constrained to ≤12 or 15 Å, respectively, from R16 Cα in any Hfq monomer. Monte Carlo simulations were performed using the program SASSIE (33) to identify conformations of free Hfq, free *rpoS* mRNA, and the *rpoS*•Hfq complex consistent with the scattering data for each sample. The coordinates of the Hfq core were fixed during the simulations, whereas the N and C termini (amino acids 1–5 and amino acids 66–102) were allowed to move. The RNA was allowed to pivot between nucleotides 128 and 129. Whereas the residuals between the best 917 models and the experimental data for the 1:1 *rpoS*•Hfq complex showed some positive serial correlation (Durbin–Watson <2), the magnitudes of the residuals were on the order of the statistical error of the data (Fig. S5*E*). See *SI Materials and Methods* for details of the modeling.

Certain commercial equipment, instruments, materials, suppliers, or software are identified in this paper to foster understanding. Such identification does not imply recommendation or endorsement by the National Institute of Standards and Technology, nor does it imply that the materials or equipment identified are necessarily the best available for the purpose.

ACKNOWLEDGMENTS. The authors thank X. Zuo and the APS 12-ID-B staff, S. Krueger, S. Gottesman, G. Storz, and Y.-X. Wang for helpful discussion and D. Kilburn, S. Panja, N. Majdalani, N. Kim, and T. Schlick for their assistance. This work was supported by the National Institute of General Medicine (Grant R01 GM46686 to S.A.W.) and the National Cancer Institute Center for Cancer Research (Y.-X. Wang). This work benefited from CCP-SAS software developed through a joint Engineering and Physical Sciences Research Council (EP/K039121/1) and National Science Foundation (CHE-1265821) grant. Use of the Advanced Photon Source was supported by the US Department of Energy under Contract DE-AC02-06CH11357.

1. Gottesman S, et al. (2006) Small RNA regulators and the bacterial response to stress. *Cold Spring Harb Symp Quant Biol* 71:1–11.
2. Michaux C, Verneuil N, Hartke A, Giard JC (2014) Physiological roles of small RNA molecules. *Microbiology* 160(Pt 6):1007–1019.
3. Storz G, Opdyke JA, Zhang A (2004) Controlling mRNA stability and translation with small, noncoding RNAs. *Curr Opin Microbiol* 7(2):140–144.
4. Vogel J, Luisi BF (2011) Hfq and its constellation of RNA. *Nat Rev Microbiol* 9(8): 578–589.
5. Mura C, Randolph PS, Patterson J, Cozen AE (2013) Archaeal and eukaryotic homologs of Hfq: A structural and evolutionary perspective on Sm function. *RNA Biol* 10(4): 636–651.
6. Sauer E (2013) Structure and RNA-binding properties of the bacterial LSm protein Hfq. *RNA Biol* 10(4):610–618.
7. Link TM, Valentin-Hansen P, Brennan RG (2009) Structure of *Escherichia coli* Hfq bound to polyriboadenylate RNA. *Proc Natl Acad Sci USA* 106(46):19292–19297.
8. Mikulecky PJ, et al. (2004) Escherichia coli Hfq has distinct interaction surfaces for DsrA, rpoS and poly(A) RNAs. *Nat Struct Mol Biol* 11(12):1206–1214.
9. Lorenz C, et al. (2010) Genomic SELEX for Hfq-binding RNAs identifies genomic aptamers predominantly in antisense transcripts. *Nucleic Acids Res* 38(11):3794–3808.
10. Sauer E, Weichenrieder O (2011) Structural basis for RNA 3′-end recognition by Hfq. *Proc Natl Acad Sci USA* 108(32):13065–13070.
11. Schumacher MA, Pearson RF, Møller T, Valentin-Hansen P, Brennan RG (2002) Structures of the pleiotropic translational regulator Hfq and an Hfq-RNA complex: A bacterial Sm-like protein. *EMBO J* 21(13):3546–3556.
12. Ishikawa H, Otaka H, Maki K, Morita T, Aiba H (2012) The functional Hfq-binding module of bacterial sRNAs consists of a double or single hairpin preceded by a U-rich sequence and followed by a 3′ poly(U) tail. *RNA* 18(5):1062–1074.
13. Otaka H, Ishikawa H, Morita T, Aiba H (2011) PolyU tail of rho-independent terminator of bacterial small RNAs is essential for Hfq action. *Proc Natl Acad Sci USA* 108(32):13059–13064.
14. Sauer E, Schmidt S, Weichenrieder O (2012) Small RNA binding to the lateral surface of Hfq hexamers and structural rearrangements upon mRNA target recognition. *Proc Natl Acad Sci USA* 109(24):9396–9401.
15. Panja S, Schu DJ, Woodson SA (2013) Conserved arginines on the rim of Hfq catalyze base pair formation and exchange. *Nucleic Acids Res* 41(15):7536–7546.
16. Battesti A, Majdalani N, Gottesman S (2011) The RpoS-mediated general stress response in Escherichia coli. *Annu Rev Microbiol* 65:189–213.
17. Lease RA, Cusick ME, Belfort M (1998) Riboregulation in *Escherichia coli*: DsrA RNA acts by RNA:RNA interactions at multiple loci. *Proc Natl Acad Sci USA* 95(21): 12456–12461.
18. Majdalani N, Cunning C, Sledjeski D, Elliott T, Gottesman S (1998) DsrA RNA regulates translation of RpoS message by an anti-antisense mechanism, independent of its action as an antisilencer of transcription. *Proc Natl Acad Sci USA* 95(21):12462–12467.
19. Soper T, Mandin P, Majdalani N, Gottesman S, Woodson SA (2010) Positive regulation by small RNAs and the role of Hfq. *Proc Natl Acad Sci USA* 107(21):9602–9607.
20. Soper TJ, Woodson SA (2008) The rpoS mRNA leader recruits Hfq to facilitate annealing with DsrA sRNA. *RNA* 14(9):1907–1917.
21. Lease RA, Woodson SA (2004) Cycling of the Sm-like protein Hfq on the DsrA small regulatory RNA. *J Mol Biol* 344(5):1211–1223.
22. Soper TJ, Doxzen K, Woodson SA (2011) Major role for mRNA binding and restructuring in sRNA recruitment by Hfq. *RNA* 17(8):1544–1550.
23. Updegrove T, Wilf N, Sun X, Wartell RM (2008) Effect of Hfq on RprA-rpoS mRNA pairing: Hfq-RNA binding and the influence of the 5′ rpoS mRNA leader region. *Biochemistry* 47(43):11184–11195.
24. Peng Y, Soper TJ, Woodson SA (2014) Positional effects of AAN motifs in rpoS regulation by sRNAs and Hfq. *J Mol Biol* 426(2):275–285.
25. Chamberlin SI, Weeks KM (2000) Mapping local nucleotide flexibility by selective acylation of 2′-amine substituted RNA. *J Am Chem Soc* 122(2):216–224.
26. Hämmerle H, Večerek B, Resch A, Bläsi U (2013) Duplex formation between the sRNA DsrA and rpoS mRNA is not sufficient for efficient RpoS synthesis at low temperature. *RNA Biol* 10(12):1834–1841.
27. Steen KA, Rice GM, Weeks KM (2012) Fingerprinting noncanonical and tertiary RNA structures by differential SHAPE reactivity. *J Am Chem Soc* 134(32):13160–13163.
28. Updegrove TB, Wartell RM (2011) The influence of Escherichia coli Hfq mutations on RNA binding and sRNA•mRNA duplex formation in rpoS riboregulation. *Biochim Biophys Acta* 1809(10):532–540.
29. Beich-Frandsen M, et al. (2011) Structural insights into the dynamics and function of the C-terminus of the E. coli RNA chaperone Hfq. *Nucleic Acids Res* 39(11):4900–4915.
30. Henderson CA, et al. (2013) Hfq binding changes the structure of Escherichia coli small noncoding RNAs OxyS and RprA, which are involved in the riboregulation of rpoS. *RNA* 19(8):1089–1104.
31. Durand D, et al. (2010) NADPH oxidase activator p67(phox) behaves in solution as a multidomain protein with semi-flexible linkers. *J Struct Biol* 169(1):45–53.
32. Wang W, et al. (2011) Cooperation of Escherichia coli Hfq hexamers in DsrA binding. *Genes Dev* 25(19):2106–2117.
33. Curtis JE, Raghunandan S, Nanda H, Krueger S (2012) SASSIE: A program to study intrinsically disordered biological molecules and macromolecular ensembles using experimental scattering restraints. *Comput Phys Commun* 183(2):382–389.
34. Parisien M, Major F (2008) The MC-Fold and MC-Sym pipeline infers RNA structure from sequence data. *Nature* 452(7183):51–55.
35. Petoukhov MV, Svergun DI (2005) Global rigid body modeling of macromolecular complexes against small-angle scattering data. *Biophys J* 89(2):1237–1250.
36. Salim NN, Feig AL (2010) An upstream Hfq binding site in the fhlA mRNA leader region facilitates the OxyS-fhlA interaction. *PLoS ONE* 5(9):e13028.
37. Salvail H, Caron MP, Bélanger J, Massé E (2013) Antagonistic functions between the RNA chaperone Hfq and an sRNA regulate sensitivity to the antibiotic colicin. *EMBO J* 32(20):2764–2778.

Supporting Information

Peng et al. 10.1073/pnas.1410114111

SI Materials and Methods

SHAPE Footprinting. Complexes of *E. coli* Hfq protein, *rpoS301* RNA, and DsrA sRNA were assembled in 10 μL annealing buffer (50 mM Tris·HCl, pH 7.5, 50 mM NaCl, 50 mM KCl, 50 mM NH_4Cl, 2% glycerol) at 25 °C for 2 h. Reactions contained 50 nM *rpoS301* plus 200 nM DsrA and 333 nM Hfq hexamer as stated in the text. Complexes were modified for 2 h at 37 °C with 1 μL 20 mM *N*-methylisatoic anhydride (Molecular Probes) dissolved in anhydrous DMSO and then analyzed by reverse transcription as previously described (1). cDNA products were quantified using SAFA (2) and normalized to reference bands that showed constant intensity in different lanes of the gel (3). The SHAPE reactivity of *rpoS* RNA complexes relative to *rpoS* RNA alone was calculated from the ratios of adjusted band intensities and ranged from 0.15 to 8.88 (Fig. S1*D*). Outliers with values 30–100 times above the background usually occurred next to very strong RT pauses and were manually excluded from the data. Each SHAPE reactivity profile is the average of at least three independent experiments. Error bars represent the SD from the mean. A histogram for the entire dataset was constructed with bin sizes equal to the average SD of the SHAPE reactivity, and the nucleotides were grouped and colored as illustrated in Fig. S1*D*. Secondary structure schemes were prepared with xrna (rna.ucsc.edu/rnacenter/xrna/xrna.html).

SAXS. Hfq was purified as previously described (4). Concentrated protein was dialyzed twice against SAXS buffer (annealing buffer plus 2 mM $MgCl_2$) at a final concentration of 1.90 mg/mL (170 μM monomer). *rpoS301* RNA was purified by a native 6% polyacrylamide gel in 1× THEM2, eluted from the gel overnight at 4 °C in SAXS buffer, concentrated by ultrafiltration (Amicon Ultra-15 centrifugal filter unit, 50 kDa), and washed five times with fresh SAXS buffer (5). The final concentration was 0.43 mg/mL (4.6 μM). Samples were shipped on ice and stored at 4 °C before use. Remaining SAXS buffer from the sample preparation was used for diluting samples and measuring background scattering. Small-angle X-ray scattering data were collected at the Advanced Photon Source 12-ID-B, over the range $0.005 < q < 1.007$ $Å^{-1}$ as described previously (5). Guinier fits and real space inversions were done using Primus and GNOM from the ATSAS software package (6). Other plots were generated using the ScÅtter software package (bl1231.als.lbl.gov/scatter). SAXS data collected on fresh samples with different concentrations showed constant R_g and ratios of scattering intensity, indicating a lack of interparticle interactions (Fig. S4), although dynamic light scattering of frozen samples showed ∼11% scattering from an RNA dimer. Estimates of the molecular mass by the method of Rambo and Tainer (7) were within 10% of the nominal value (Table S2). The disordered C terminus of Hfq may result in higher than expected estimates by this method (8).

MC-Sym. Three-dimensional models of *rpoS* mRNA secondary structure fragments (Fig. S7) were generated using MC-Sym web server (9). The RNA sequence and secondary structure based on SHAPE experiments were used as the input with default settings; two-stranded fragments were first connected with a GAAA tetraloop. The output structures were ranked using the MC-Sym web server tools. The top five predicted structures for each fragment did not differ substantially. The highest-scoring structure for each fragment was selected for rigid-body modeling, after removal of GAAA tetraloops and energy minimization with UCSF Chimera (10). The predicted structures were consistent with the experimental SHAPE data, with highly modified residues occurring in hairpin loops or kinks in the RNA backbone (Fig. S7). The "hinge" region of the structure (light blue in Fig. S7) is the least well determined, but even the model for this region is in reasonable agreement with the data. The two three-helix junctions (type C) (11) were also predicted using a knowledge-based method (12–14). This method returned the same stacking geometry as in our model for the inhibitory stem-loop domain (pink in Fig. S7), but a slightly different stacking geometry for the upstream three-helix junction (red in Fig. S7).

Rigid-Body Modeling of *rpoS* and *rpoS*•Hfq Complex. The tertiary structure of *rpoS* RNA was modeled by orienting the RNA fragments by rigid-body modeling (SASREF) (15), using the SAXS experimental data as a constraint ($\chi^2 = 0.59$). The RNA connectivity was enforced by setting the distance between adjacent phosphorous atoms to ≤7 Å (res 40–41, 57–58, and 127–128). To allow more flexibility in the fitting procedure, the distance between connecting phosphorus atoms was constrained to ≤8 Å in only one of the two strands in the inhibitory stem (res 162–163 or res 272–273 for connecting fragments 4 and 5, and res 184–185 or res 248–249 for connecting fragments 5 and 6). Because we could not model single-stranded regions of the upstream domain (res 73–86 and res 102–116) with MC-Sym, the missing sequences were initially built assuming an A-form conformation, and all of the fragments were manually connected into a continuous strand in UCSF Chimera (10). Structures resulting from repeated calculations were similar, with two structural domains oriented at ∼90°. The predicted structures were not sensitive to changes in distance constraints.

CORAL was used to model the full *rpoS*•Hfq complex against the SAXS data for the 1:1 RNA:Hfq sample (16). An initial model of Hfq core bound to the AAN_4 motif was obtained by importing the coordinates of six protomers of *E. coli* $Hfq_{5–65}$ in complex with A_7 RNA (PDB ID: 4HT8) (17). To this model, we added the missing C termini of Hfq (resi 66–102) and the *rpoS* fragments used for SASREF modeling of free *rpoS* RNA with the same contact restraints. The A7 RNA bound to Hfq was joined to the rest of the RNA by setting the distance between *rpoS301* P 88 and the 3′ end of A7 ≤7 Å. Two additional constraints were introduced based on the SHAPE footprinting data: *rpoS301* P 195 (U_5 motif) ≤12 Å from the α-carbon of R16 in any Hfq monomer and *rpoS301* P157 (inhibitory stem) ≤15 Å from R16 α-carbon in any Hfq monomer. Finally, the missing nucleotides (nucleotides 73–80 and 102–116) were built and connected manually in UCSF Chimera.

Monte Carlo Simulations of Hfq, *rpoS*, and Hfq•*rpoS* Complexes by SASSIE. Monte Carlo simulations (SASSIE) (18) were used to identify conformations of free Hfq, free *rpoS* mRNA, and the *rpoS*•Hfq complex consistent with the scattering data for each sample. The coordinates of the Hfq core (alone or with rA bound to the distal face) (17) were fixed during the simulations, whereas the N- and C-terminal residues (res 1–5 and res 66–102) were allowed to vary. The initial full-length Hfq structure was energy minimized using CHARMM (19), before it was used as the input for the Monte Carlo simulation. During the Monte Carlo simulation, Crysol 2.7 (20) was used to calculate scattering profiles of simulated structures after renaming atoms to C, H, N, O, P, S to avoid reading errors in Crysol. The averaged SAXS profile of Hfq was interpolated (43 points, $\Delta q = 0.005$ from 0.005

to 0.21) and was used to evaluate the theoretical scattering profiles. Models generated by SASSIE that best fitted the experimental SAXS data were minimized using CHARMM.

The free *rpoS* structure generated by rigid-body modeling was modeled using SASSIE as described above. However, the RNA was allowed to pivot around the flexible hinge connecting the upstream and downstream domains (res 128–129). The Monte Carlo dihedral sampling of RNA backbone configurations was carried out using CHARMM 36 force-field parameters (21) for α, β, γ, δ, ε, η angles, using the same energetic sampling as described previously (18).

The RNA coordinates of the *rpoS*•Hfq complex generated from rigid-body modeling and the full-length Hfq structure generated from SASSIE were merged into a starting structure for Monte Carlo simulations of the complex. CHARMM was used to minimize the energy in three steps by first restraining all RNA atoms, then restraining the RNA carbon and phosphate atoms, and then allowing all atoms to move. A SASSIE Monte Carlo simulation was carried out as above, using *rpoS* res 128–129 as a pivot point and allowing Hfq N and C termini to vary. The SAXS profile of the 1:1 *rpoS*•Hfq sample was used to evaluate the theoretical scattering profiles, using χ^2 (Eq. **S1**) as a measure of statistical goodness-of-fit,

$$\chi^2 = \frac{1}{(N-1)} \sum_{Q_i} \frac{\left(I_{\exp}(Q_i) - I_{\text{calc}}(Q_i)\right)^2}{\sigma_{\exp}(Q_i)^2}, \qquad \textbf{[S1]}$$

in which $I_{\exp}(Q_i)$ is the experimentally determined SAXS scattering curve, $I_{\text{calc}}(Q_i)$ is the value obtained using SASSIE, $\sigma_{\exp}(Q_i)$ is the experimentally determined Q-dependent variance, and the sum was taken over $i = 1$ to N, with $n = 43$ grid points of momentum transfer Q. Some values of $\chi^2 < 1$, indicating that either our estimate of $\sigma_{\exp}(Q_i)$ is too large or more likely that the there are fewer than $N - 1$ df in our dataset. To account for variance in the value of χ^2 ($3\sigma \sim \pm 0.66$) given the limited number of data points and the uncertainty in the true number of degrees of freedom in the data, we arbitrarily considered all models with $\chi^2 < 1.5$, which span the experimentally determined R_g value. An alternative measure of error $V(r)$ (7) reached a minimum around a similar range of R_g values (Fig. S6). The best-fit structures were energy minimized using CHARMM. Final models were compared with the scattering data, using FoXS (22).

1. Peng Y, Soper TJ, Woodson SA (2012) RNase footprinting of protein binding sites on an mRNA target of small RNAs. *Methods Mol Biol* 905:213–224.
2. Das R, Laederach A, Pearlman SM, Herschlag D, Altman RB (2005) SAFA: Semi-automated footprinting analysis software for high-throughput quantification of nucleic acid footprinting experiments. *RNA* 11(3):344–354.
3. Behrouzi R (2012) The roles of native tertiary interactions in the folding pathway of the Azoarcus ribozyme. PhD thesis (ProQuest Dissertations and Theses, Johns Hopkins University, Baltimore).
4. Soper TJ, Doxzen K, Woodson SA (2011) Major role for mRNA binding and restructuring in sRNA recruitment by Hfq. *RNA* 17(8):1544–1550.
5. Fang X, et al. (2013) An unusual topological structure of the HIV-1 Rev response element. *Cell* 155(3):594–605.
6. Konarev PV, Volkov VV, Sokolova AV, Koch MHJ, Svergun DI (2003) PRIMUS: A Windows PC-based system for small-angle scattering data analysis. *J Appl Cryst* 36(5): 1277–1282.
7. Rambo RP, Tainer JA (2013) Accurate assessment of mass, models and resolution by small-angle scattering. *Nature* 496(7446):477–481.
8. Watson MC, Curtis JE (2014) Probing the average local structure of biomolecules using small-angle scattering and scaling laws. *Biophys J* 106(11):2474–2482.
9. Parisien M, Major F (2008) The MC-Fold and MC-Sym pipeline infers RNA structure from sequence data. *Nature* 452(7183):51–55.
10. Pettersen EF, et al. (2004) UCSF Chimera—a visualization system for exploratory research and analysis. *J Comput Chem* 25(13):1605–1612.
11. Lescoute A, Westhof E (2006) Topology of three-way junctions in folded RNAs. *RNA* 12(1):83–93.
12. Kim N, et al. (2014) Graph-based sampling for approximating global helical topologies of RNA. *Proc Natl Acad Sci USA* 111(11):4079–4084.
13. Laing C, Schlick T (2009) Analysis of four-way junctions in RNA structures. *J Mol Biol* 390(3):547–559.
14. Laing C, Wen D, Wang JT, Schlick T (2012) Predicting coaxial helical stacking in RNA junctions. *Nucleic Acids Res* 40(2):487–498.
15. Petoukhov MV, Svergun DI (2005) Global rigid body modeling of macromolecular complexes against small-angle scattering data. *Biophys J* 89(2):1237–1250.
16. Petoukhov MV, et al. (2012) New developments in the ATSAS program package for small-angle scattering data analysis. *J Appl Cryst* 45(2):342–350.
17. Wang W, et al. (2011) Cooperation of Escherichia coli Hfq hexamers in DsrA binding. *Genes Dev* 25(19):2106–2117.
18. Curtis JE, Raghunandan S, Nanda H, Krueger S (2012) SASSIE: A program to study intrinsically disordered biological molecules and macromolecular ensembles using experimental scattering restraints. *Comput Phys Commun* 183(2):382–389.
19. Brooks BR, et al. (2009) CHARMM: The biomolecular simulation program. *J Comput Chem* 30(10):1545–1614.
20. Svergun DI, Barberato C, Koch MHJ (1995) CRYSOL - a program to evaluate X-ray solution scattering of biological macromolecules from atomic coordinates. *J Appl Cryst* 28:768–773.
21. Foloppe N, MacKerell JAD (2000) All-atom empirical force field for nucleic acids: I. Parameter optimization based on small molecule and condensed phase macromolecular target data. *J Comput Chem* 21(2):86–104.
22. Schneidman-Duhovny D, Hammel M, Tainer JA, Sali A (2013) Accurate SAXS profile computation and its assessment by contrast variation experiments. *Biophys J* 105(4): 962–974.

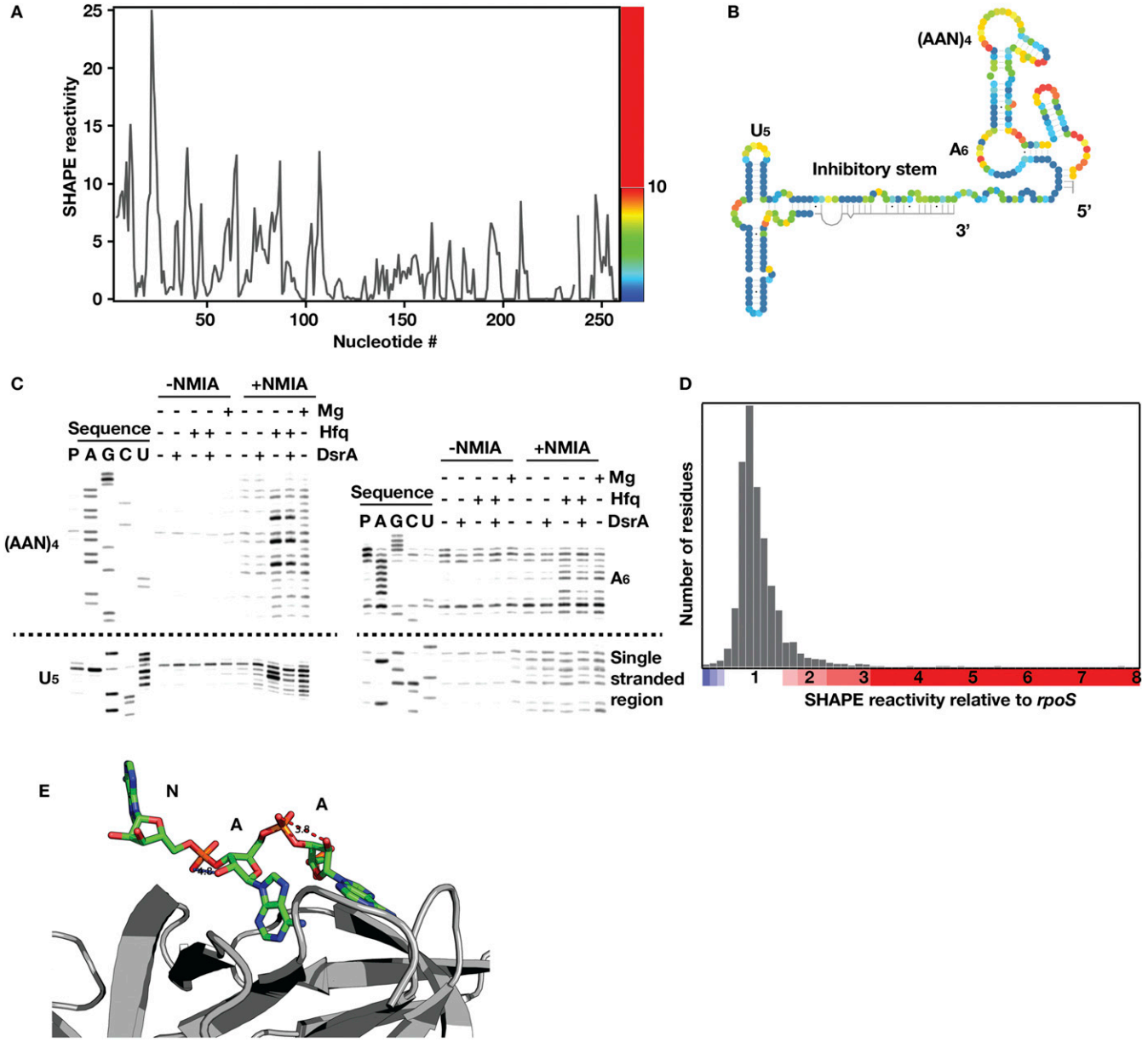

Fig. S1. SHAPE footprinting of *rpoS* mRNA with sRNA and Hfq. (*A*) Modification of ribose 2′OH was quantified by primer extension and analyzed by sequencing gel electrophoresis. To determine the overall secondary structure, traces from primer extensions covering different regions of the *rpoS301* RNA were overlapped. (*B*) rpoS301 secondary structure consistent with experimental SHAPE modification data (colors). The linker between the upstream and downstream domains is predicted by MC-Sym to fold into a short stem loop, in agreement with its low reactivity. Gray, no data. (*C*) Selected sequencing gel images showing hyperreactive residues induced by Hfq binding at the $(AAN)_4$ motif (*Top Left*) and the U_5 motif (*Bottom Left*). Hfq also opens the secondary structure at the A_6 motif (*Top Right*) but does not affect other single-stranded regions (*Bottom Right*). (*D*) Histogram of SHAPE reactivity relative to *rpoS* RNA for the entire dataset. Values below 0.6 (~3% of nucleotides) were considered protected; values above 1.75 were considered enhanced (~10% of nucleotides). Nucleotides were clustered based on their relative SHAPE reactivity: dark to light blue, protected, 0.140–0.287 (~0.2%), 0.287–0.434 (~0.3%), and 0.434–0.581 (~0.6%); white, unchanged, 0.728–1.757 (~87.1%); and light to dark red, enhanced, 1.757–2.051 (~4.5%), 2.051–2.639 (~3.4%), 2.639–3.521 (~1.5%), and 3.521–8.813 (~0.8%). RNA secondary structure schematics were drawn with XRNA (rna.ucsc.edu/rnacenter/xrna/xrna.html). (*E*) Structure of AAN triple bound to the distal face of Hfq (PDB ID: 3GIB) showing the short 3.8-Å distance between the first 2′OH and the phosphate of the second A. This conformation is associated with strong reactivity toward electrophiles used for SHAPE chemistry (1).

1. Steen KA, Rice GM, Weeks KM (2012) Fingerprinting noncanonical and tertiary RNA structures by differential SHAPE reactivity. *J Am Chem Soc* 134(32):13160–13163.

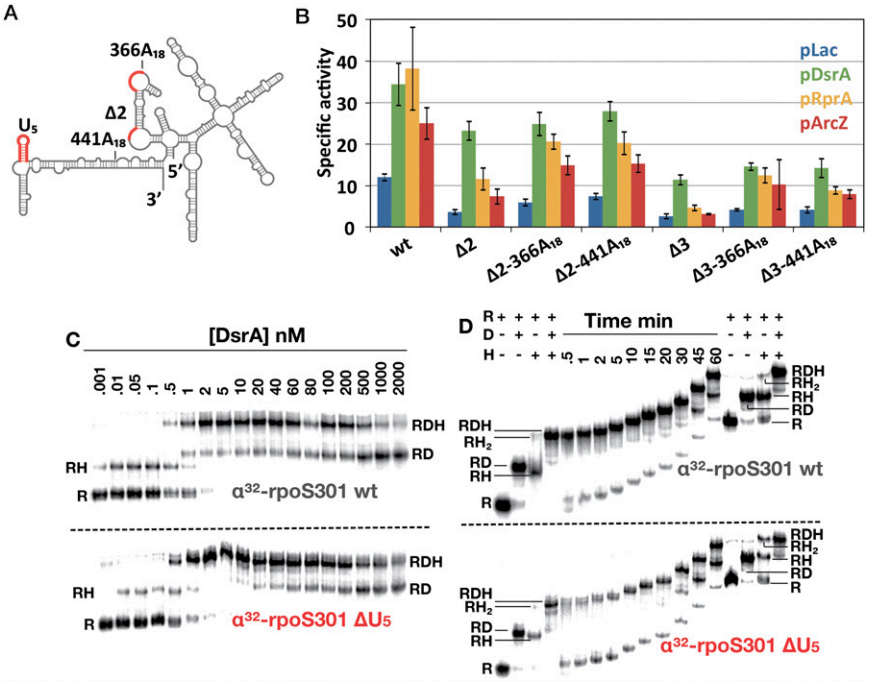

Fig. S2. The U5 motif functions independently of the AAN motif. (*A* and *B*) Full-length *rpoS* leader (576 nt) fused to *lacZ* was used to measure in vivo expression of β-galactosidase as in Fig. 3*B*. Δ2, upstream $(AAN)_4$ and A_6 motifs were replaced with GC-rich sequence (1); Δ3, ΔU_5 plus Δ2 mutation; $366A_{18}$ and $441A_{18}$, an A18 insertion at positions 366 and 441 to rescue Δ2 *rpoS* function (2). (*C* and *D*) Native polyacrylamide gel mobility shift assay for DsrA binding to rpoS mRNA. (*C*) Equilibrium binding at different DsrA concentrations. Fraction bound was calculated from counts in each lane in *rpoS*•DsrA (RD) or *rpoS*•DsrA•Hfq (RDH) bands. (*D*) Binding kinetics, as in *C*. Samples were loaded at various times during electrophoresis.

1. Soper T, Mandin P, Majdalani N, Gottesman S, Woodson SA (2010) Positive regulation by small RNAs and the role of Hfq. *Proc Natl Acad Sci USA* 107(21):9602–9607.
2. Peng Y, Soper TJ, Woodson SA (2014) Positional effects of AAN motifs in rpoS regulation by sRNAs and Hfq. *J Mol Biol* 426(2):275–285.

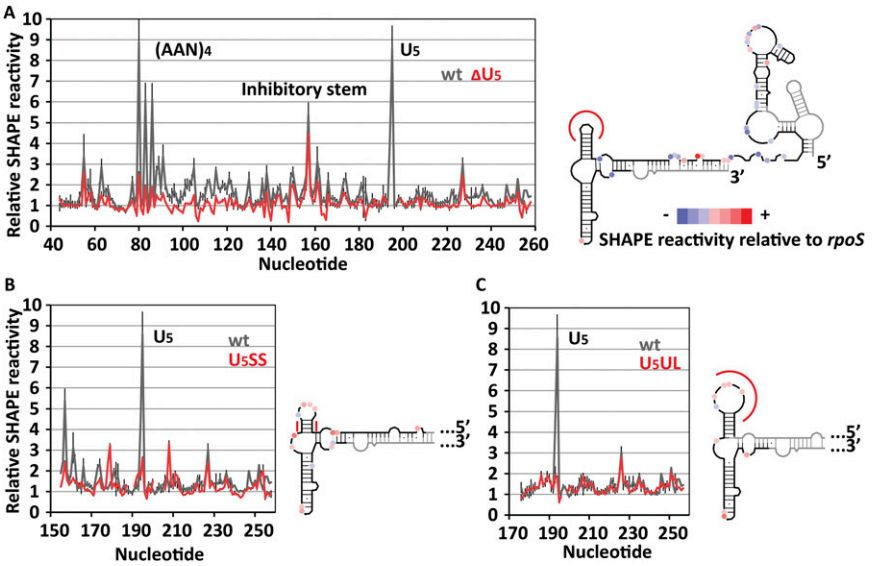

Fig. S3. (*A*–*C*) Hfq specifically recognizes the U_5 motif. Shown is comparison of relative SHAPE reactivity of WT *rpoS*•Hfq complex (gray trace) and U_5 mutant *rpoS*•Hfq complexes (red trace). Mutations (highlighted in red lines) are as shown in Fig. 3*A*. These mutations were predicted by MFOLD (1) not to alter the rest of the RNA secondary structure.

1. Zuker M (2003) Mfold web server for nucleic acid folding and hybridization prediction. *Nucleic Acids Res* 31(13):3406–3415.

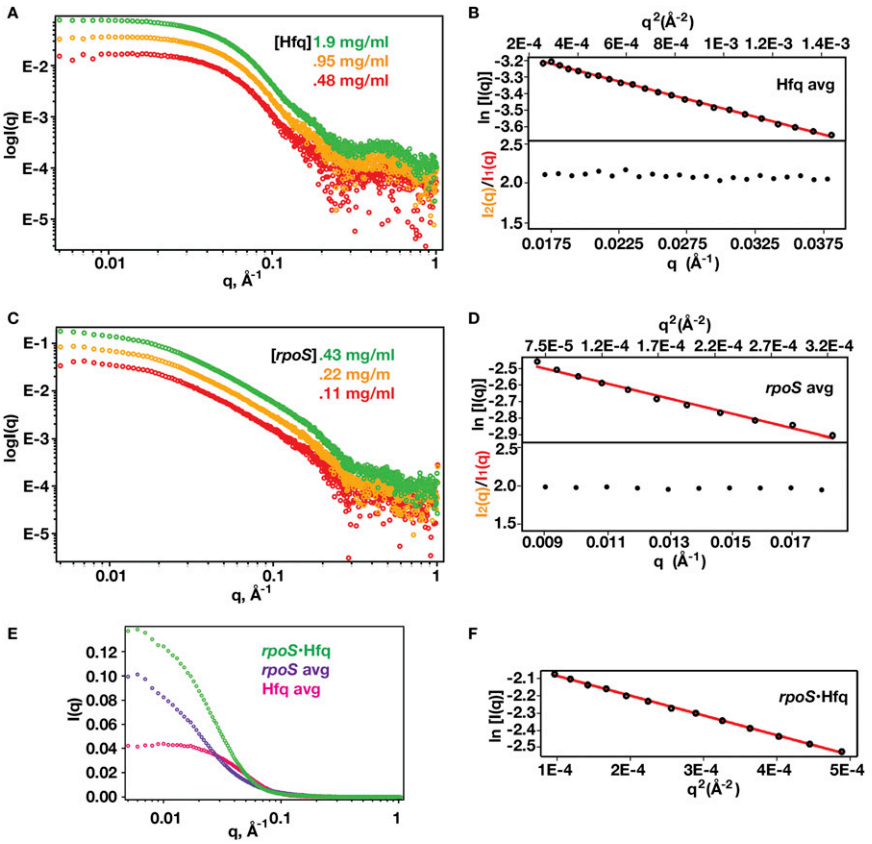

Fig. S4. Solution scattering of Hfq and *rpoS* mRNA. Shown are SAXS scattering profiles of (*A* and *B*) full-length Hfq and (*C* and *D*) *rpoS301* RNA at three concentrations (colored green, orange, and red) in solution. (*B* and *D*, *Top*) Guinier plot of averaged data for free Hfq and free *rpoS*301 RNA. (*Bottom*) The ratio of scattering intensity from two Hfq or RNA concentrations remained constant over the Guinier region, confirming the absence of interparticle interactions (shown here for the lowest two concentrations that differ by a factor of 2). (*E*) The averaged scattering curves for Hfq (magenta), *rpoS* RNA (purple), and 1:1 *rpoS*•Hfq complex (green) were used to calculate R_g from the Guinier region (33.6 ± 0.5 Å, 68.1 ± 1.6 Å, and 58.0 ± 1.0 Å, respectively). (*F*) Guinier plot of 1:1 *rpoS*•Hfq complex.

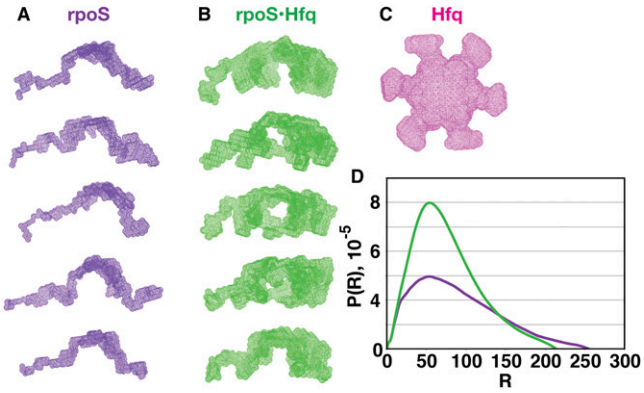

Fig. S5. Ab initio models of *rpoS* RNA, Hfq protein, and the *rpoS*•Hfq complex. (*A* and *B*) Five ab initio structures predicted by DAMMIF for (*A*) free *rpoS* RNA and (*B*) the *rpoS*•Hfq complex (1:1 molar ratio). The *rpoS* envelopes adopt an extended L-shaped conformation, consistent with the all-atom model (Fig. 5). Hfq binding folds *rpoS* RNA into a more compact conformation. DAMMIF assumes the electron density is evenly distributed in the complex and does not account for differential SAXS scattering intensity from Hfq protein and *rpoS* mRNA. As a result, the space occupied by Hfq protein appears empty in the molecular envelope. Averaging these ab initio models resulted in a significant loss of structural detail. (*C*) The averaged ab initio model of Hfq predicted by DAMAVER (1) is very similar to previous models based on SAXS data (2, 3), which assumed oblate P6 symmetry. Twenty DAMMIF bead models were averaged and DAMMIN was restarted to fit the experimental data. (*D*) *P*(*R*) distribution of free *rpoS* RNA (purple) and the *rpoS*•Hfq complex (green), showing the change in the average conformation of the particle. The mass of the RNA and Hfq particles was calculated from the molecular volume, Vc, using the method of Rambo and Tainer (4). Real space parameters for the scattering data are given in Table S2.

1. Volkov VV, Svergun DI (2003) Uniqueness of ab initio shape determination in small-angle scattering. *J Appl Cryst* 36(3 Part 1):860–864.
2. Beich-Frandsen M, Večerek B, Sjöblom B, Bläsi U, Djinović-Carugo K (2011) Structural analysis of full-length Hfq from Escherichia coli. *Acta Crystallogr Sect F Struct Biol Cryst Commun* 67 (Pt 5):536–540.
3. Henderson CA, et al. (2013) Hfq binding changes the structure of Escherichia coli small noncoding RNAs OxyS and RprA, which are involved in the riboregulation of rpoS. *RNA* 19(8): 1089–1104.
4. Rambo RP, Tainer JA (2013) Accurate assessment of mass, models and resolution by small-angle scattering. *Nature* 496(7446):477–481.

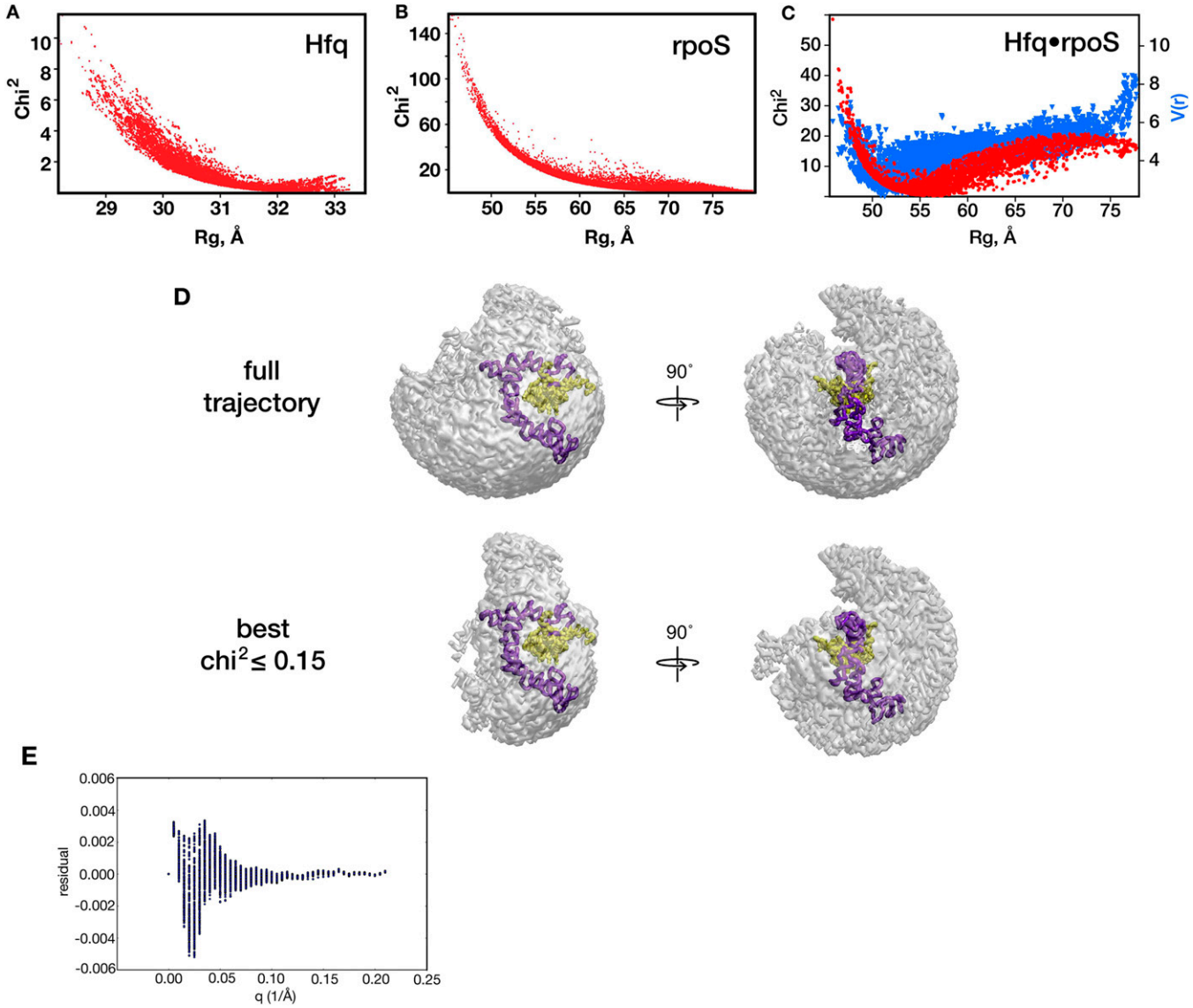

Fig. S6. Monte Carlo and molecular dynamics simulations of free Hfq and *rpoS* RNA. (*A–C*) Comparison of experimental SAXS data with Monte Carlo simulations of (*A*) Hfq (24,991 structures), (*B*) free *rpoS* mRNA (27,427 structures), and (*C*) *rpoS*•Hfq complex (19,132 structures), performed with the program SASSIE (18). In *A*, the conformations of the intrinsically disordered N- and C-terminal residues were varied until the space around the hexamer core was fully sampled. (*B* and *C*) Residues 128–129 were used as a pivot point to produce an ensemble of structures spanning the experimental R_g for the free RNA (68.1 Å) and the complex (58 Å). The metric *Vr* (7) (blue in *C*) reaches a minimum at similar R_g values to χ^2, but is less sensitive to variations in the structures. The "best-fit" structure in this ensemble is depicted as an example of the "open" conformation of the *rpoS*•Hfq complex (Fig. 5*E*). (*D*) Spatial distribution of downstream *rpoS* mRNA domain in simulated Hfq•*rpoS* RNA structures (gray surface). Models were aligned to Hfq and superimposed. One conformation in the trajectory is shown as a ribbon; RNA, violet; Hfq, yellow. (*Top*) In the full trajectory, the downstream *rpoS* mRNA domain sampled the entire space around the Hfq Sm core. (*Bottom*) Structures that best match the experimental SAXS data ($\chi^2 \leq 1.5$) are confined to a wedge of space around the proximal face of Hfq, as also shown in Fig. 5*G*. (*E*) A plot of the residual (calculated profile minus experimental profile) for each of the 917 structures of the complex with $\chi^2 \leq 1.5$. Although some positive serial correlation was observed (Durbin–Watson statistical test <2), the magnitude of the residuals was on the order of the statistical error of the data.

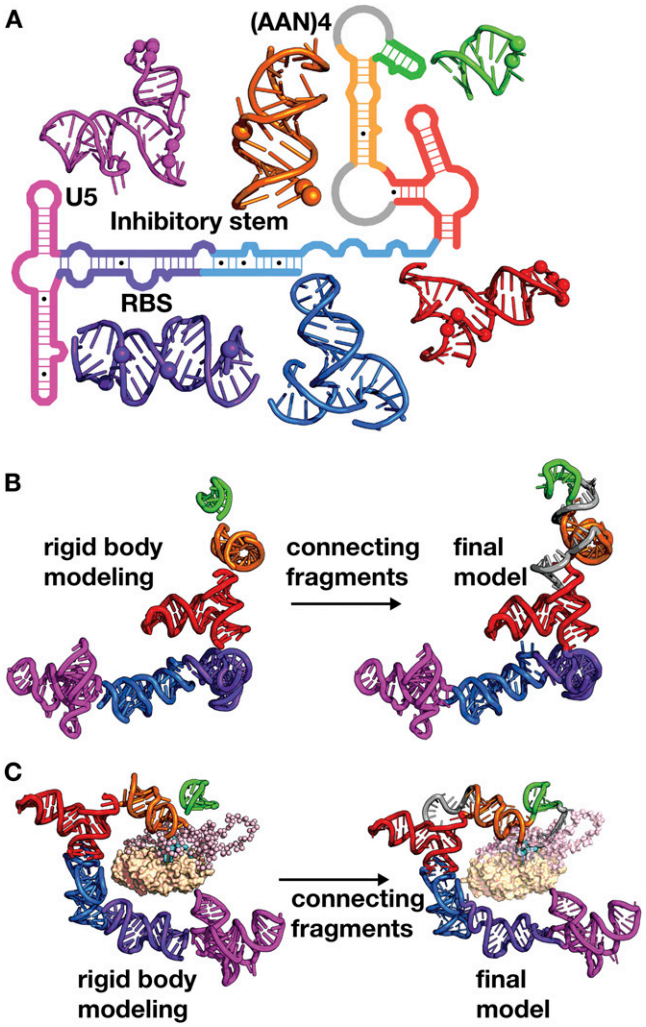

Fig. S7. Tertiary structures of rpoS301 fragments predicted by MC-Sym. (*A*) Using the SHAPE-determined secondary structure as a guide (Fig. S1), *rpoS301* was divided into six fragments. The tertiary structure of each fragment was predicted by MC-Sym (9): an upstream four-way junction (red), a long helix connecting the $(AAN)_4$ motif and A_6 loops (orange), a short hairpin next to the $(AAN)_4$ motif (green), a linker region (blue), the inhibitory stem (purple), and the downstream four-way junction containing the U_5 motif (magenta). The single-stranded $(AAN)_4$ and A_6 motifs were assumed to be unstructured linkers, based on moderate SHAPE reactivity (gray). The predicted secondary structures were consistent with SHAPE modification (Fig. S1). Highly modified nucleotides are shown as spheres on the ribbons. (*B*) SASREF rigid-body model of free *rpoS* RNA. (*Left*) Initial output of SASREF with disconnected fragments arranged to satisfy proximity constraints and the experimental SAXS scattering. (*Right*) Final models were built after filling in missing fragments and connecting adjacent RNA modules. (*C*) CORAL rigid-body model of the *rpoS*•Hfq complex, as in *B*.

Table S1. Summary of *rpoS*•DsrA binding constants and annealing rate constants

	DsrA K_d, nM		DsrA annealing rate, min^{-1}		
rpoS	–Hfq	+Hfq	–Hfq (%)	+Hfq, fast (%)	+Hfq, slow (%)
WT	26 ± 2	0.7 ± 0.1	0.026 ± 0.005 (98)	6.3 ± 1.3 (66)	0.06 ± 0.01 (26)
ΔU_5	23 ± 2	0.32 ± 0.04	0.031 ± 0.006 (94)	5 ± 3 (40)	0.07 ± 0.02 (50)

Shown are binding equilibria and rate constants measured by native polyacrylamide gel electrophoresis, based on data in Fig. 3 *C* and *D*. Experiments were without Hfq or with 0.6 μM Hfq monomer. The binding constants were calculated from DsrA titrations; rate constants were obtained from the formation of DsrA•*rpoS* RNA binary complex plus DsrA•*rpoS*•Hfq ternary complex over time. Values ± SD are based on three or more independent trials. Amplitudes of kinetic phases are given in parentheses.

Table S2. SAXS parameters for Hfq protein and rpoS mRNA

		Guinier				Real space					Mass, Da	
Sample	μM	R_g, Å	±	I(0)	±	R_g, Å	±	I(0)	±	R_{max}	SAXS	Nominal
Hfq	42.4	32.3	0.7	1.86*E*-02	4.6*E*-04	32.8	0.8	1.90*E*-02	3.0*E*-04	110	73,762	66,996
	84.8	33.7	0.9	3.95*E*-02	5.4*E*-04	34.0	0.4	3.95*E*-02	4.0*E*-04	120	76,975	66,996
	170	34.3	0.6	8.05*E*-02	6.1*E*-04	35.2	0.3	8.10*E*-02	5.0*E*-04	130	80,271	66,996
Hfq avg		33.6	0.5	4.45*E*-02		34.2	0.4	4.40*E*-02	4.0*E*-04	120	77,332	66,996
rpoS RNA	1.2	63.8	2.0	3.95*E*-02	1.3*E*-03	72.0	2.0	4.20*E*-02	1.2*E*-03	250	102,027	96,209
	2.3	63.8	1.2	7.80*E*-02	1.0*E*-03	71.5	1.4	8.20*E*-02	1.4*E*-03	250	105,402	96,209
	4.6	64.2	0.9	1.55*E*-01	2.0*E*-03	71.8	0.9	1.64*E*-01	1.8*E*-03	250	106,059	96,209
rpoS avg		66.0	1.6	8.97*E*-02	2.0*E*-03	76.7	2.7	9.60*E*-02	2.0*E*-03	300	106,642	96,209
1:1 Hfq:*rpoS*	2.3	58.0	1.0	1.38*E*-01	2.1*E*-03	61.1	0.7	1.40*E*-01	1.4*E*-03	250		163,205

SAXS data for Hfq protein, rpoS301 RNA, and 1:1 [Hfq]6:*rpoS* mixtures were acquired at room temperature over a momentum transfer range of $0.005 < q < 1.007$ Å^{-1} at APS 12-ID-B as described in *Materials and Methods*. For the 1:1 complex, the sample contained 2.3 μM RNA and 13.8 μM Hfq monomer. The *P*(*r*) real space parameters were calculated for $q = 0–0.5$, using GNOM. The particle mass was estimated from the SAXS scattering curves by the method of Rambo and Tainer (21) for $q = 0–0.3$ to reduce contributions of noise at high q.